



**Table 1 — Chemical Compositions of the Steels Investigated (wt-%)**

Steel	C	Si	Mn	P	S	Cr	Ni	Mo	V	Ti	Cu	Al	Co	C <sub>eq</sub> *
Fe37B	0.100	0.206	0.752	0.022	0.006	0.026	0.042	0.004	0.010	0.001	0.088	0.049	0.024	0.171
Fe52D	0.135	0.205	0.733	0.027	0.018	0.027	0.018	0.001	0.024	0.002	0.016	0.037	0.012	0.205
HSD	0.090	0.330	1.600	0.011	0.001	0.060	0.040	0.020	0.014	0.010	0.15	0.034	—	0.237
HSE	0.120	0.369	1.227	0.023	0.004	0.095	0.077	0.010	0.032	0.001	0.21	0.033	0.013	0.238

\*C<sub>eq</sub> (wt-%) = %C + %Mn/12 + %Si/24

work, simplified analytical models of heat flow and phase transformations are developed, and applied to laser welding of carbon manganese steels. Explicit relationships between HAZ properties and the principal process variables are obtained, and used to construct diagrams which show HAZ data for a range of carbon manganese steels, plate thicknesses and welding parameters. The diagrams provide guidance during procedure qualification testing of laser welds.

## Experimental

### Materials

Four carbon manganese constructional steels were used in the experimental trials, delivered as plates of thickness 8 mm (0.31 in.), with initial microstructures comprising ferrite and pearlite. Fe37B (A373-81, Grade 65) and Fe52D (A572-81, Grade 50) are basic carbon manganese structural steels, the latter having a higher carbon content and tensile strength. Two high-strength, thermo-mechanically processed steels, designated HSD and HSE, were also welded for comparison. Their chemical compositions, obtained by direct reading optical emission spectrometry, are given in Table 1. Samples with dimensions 350 x 150 mm (13.8 x 5.9 in.) were cut for experimental trials, and machined from one side, where necessary, to give a range of plate thickness between 4 and 8 mm (0.16 and 0.31 in.).

### Laser and Beam Delivery

A Rofin Sinar RS6000 CO<sub>2</sub> laser was used for welding. The design comprises fast axial gas flow, radio frequency excitation and a stable optical cavity. The parameters of the emitted beam were as follows: 10.6 μm wavelength, TEM<sub>20</sub> mode, 50 mm (2 in.) nominal diameter at the focusing optic, 500–6000 W power range, linear polarization. The beam was directed to the workpiece via tubes and flat gold-coated, water-cooled turning mirrors, with a path length of 10 m (32.8 ft). The beam power at the workpiece was calibrated to the laser power display

using a Lasercraft P10K calorimeter and an exposure time of 10 s. Values of power quoted refer to those measured at the workpiece. The beam was focused to a spot diameter of 0.3 mm (0.01 in.) using a molybdenum-coated, water-cooled paraboloidal copper mirror of focal length 150 mm (5.9 in.). The beam was oriented perpendicular to the workpiece surface, and the focal plane positioned coincident with the workpiece surface.

### Welding Procedure

The majority of the welding trials involved the production of melt runs of length 150 mm (5.9 in.), made transverse to the plate rolling direction in the flat position, by traversing the beam over the stationary, clamped workpiece using a CN-controlled workstation. In this way potential inconsistencies resulting from variations in joint fitup and surface contamination were eliminated. The technique provides a good simulation of the parameters required for a close-fitting square-groove butt joint. Welding was performed at room temperature. A number of butt joint welds were included in the experimental program for comparison with the melt run results.

The plane of beam polarization was oriented 45 deg to the welding direction. Power levels in the range 2–6 kW, and traverse rates in the range 0.4–4.0 m/min (16–160 in./min) were used. Helium gas was used to shield the weld bead from oxidation, and to suppress plasma formation during welding at low speeds. Shielding gas was delivered coaxially with the beam through a nozzle of internal diameter 4 mm (0.16 in.). Plasma suppression gas was delivered through a nozzle of internal diameter 3 mm (0.12 in.); the flow being oriented 45 deg to the workpiece, aligned against the welding direction, and directed at a position 1 mm ahead of the beam-material interaction point. Gas flow rates of 21 and 13 L/min were used for shielding and plasma suppression, respectively, and were measured using calibrated flow me-

ters. An operating window of laser power and welding speed giving full joint penetration welds (a weldability lobe), was thus established for each steel and plate thickness.

### Weld Assessment

Welds were sectioned transverse to the welding direction, ground, polished and etched in a 3% nital solution. The weld bead and HAZ were observed using optical microscopy. The HAZ was defined as the region bounded by the fusion line and the isotherm corresponding to the A<sub>c1</sub> temperature (the boundary between transformed and untransformed pearlite). The width of the HAZ was measured using a traveling microscope. Measurements were made on each side of the HAZ, at positions corresponding to 25, 50 and 75% of the plate thickness. The hardness of the coarse-grained HAZ adjacent to the weld interface was established in the same locations, using a diamond indenter with a load of 1 kg (2.2 lb). A number of transverse hardness profiles were made using a load of 300 g (0.7 lb), which indicated that the maximum hardness in the HAZ occurred adjacent to the fusion line.

## Mathematical Modeling

### Material Properties

A set of physical properties, determined empirically at 60% of the melting temperature (Ref. 21), was used to describe the carbon manganese steels — Table 2. Empirical relationships were used to calculate the temperature at which pearlite transforms to austenite on heating, T<sub>A1</sub>, (Ref. 22), and the melting temperature, T<sub>m</sub> (Ref. 23):

$$T_{A1} \text{ (K)} = 996 - 10.7\text{Mn} - 16.9\text{Ni} + 29.1\text{Si} + 16.9\text{Cr} + 290\text{As} + 6.38\text{W} \quad (1)$$

$$T_m \text{ (K)} = 1810 - 90\text{C} \quad (2)$$

Element symbols refer to nominal steel composition in wt-%. The compositions of all the steels were well within the ranges of validity of the above equations.

The fraction of incident power absorbed during welding,  $A$ , has a significant effect on the thermal cycles experienced in the weld and the subsequent weld properties. However, its value is generally not known accurately prior to welding, since it depends on poorly known factors such as the efficiency of plasma suppression, the amount of beam transmission through the keyhole, and the beam polarization.  $A$  has therefore been determined empirically for each weld, in the manner described below, and used in the calculation of the energy absorbed in the weld.

### The Temperature Field in the Weld

The keyhole is modeled as a rapidly moving, through-thickness line heat source, which approximates well the keyhole geometry in full joint penetration laser welding. The temperature,  $T$ , at a point in the HAZ increases rapidly from the initial value,  $T_o$ , to a peak,  $T_p$ , then decreases with a rate which can be characterized by the cooling time between  $800^\circ$  and  $500^\circ\text{C}$ ,  $\Delta t$ . The following analytical expressions can be derived for temperature profiles in the HAZ (Refs. 6 and 15), based on the thin plate analysis of Rosenthal (Ref. 1).

$$T - T_o = Aq/(vd) \cdot (4\pi\lambda\rho ct)^{-1/2} \cdot \exp - [r^2/(4at)] \quad (3)$$

$$T_p - T_o = Aq/(vd) \cdot [2/(\pi e)]^{1/2} \cdot (2\rho c t)^{-1} \quad (4)$$

$$\Delta t = [Aq/(vd)]^2 \cdot (4\pi\lambda\rho c)^{-1} \cdot [1/(773 - T_o)^2 - 1/(1073 - T_o)^2] \quad (5)$$

$T_o$  is the initial (or preheat) temperature,  $q$  is the incident beam power (W),  $A$  is the fraction of incident energy absorbed by the workpiece,  $v$  is the traverse rate (m/s),  $d$  is the plate thickness (m),  $\lambda$  is the thermal conductivity (W/m/K),  $\rho$  is the density (kg/m<sup>3</sup>),  $c$  is the heat capacity (J/kg/K),  $t$  is the time (s),  $r$  is the lateral distance from the heat source (m),  $a$  is the thermal diffusivity ( $\lambda/\rho c$ , m<sup>2</sup>/s), and  $e$  is the base of natural logarithms (2.718).

**Table 2 — Physical Properties of the Steels Investigated**

Property	Steel				Reference
	Fe37B	Fe52D	HSD	HSE	
Density (kg/m <sup>3</sup> )	7860	7860	7860	7860	Ref. 23
Thermal Conductivity (W/m/K)	30	30	30	30	Ref. 21
Specific Heat Capacity (J/kg/K)	680	680	680	680	Ref. 21
$A_{c1}$ Temperature (K)	994	994	989	994	Ref. 22
Melting Temperature (K)	1801	1798	1802	1799	Ref. 23

### Width of the HAZ

The HAZ width is a measure of the energy absorbed during welding, and hence the HAZ cooling rate. Equation 4 can be rearranged and evaluated using the isotherm positions  $r_m$  and  $r_{A1}$  corresponding to the peak temperatures  $T_m$  and  $T_{A1}$ , respectively, to give the width of the HAZ

$$r_{A1} - r_m = Aq/(vd) \cdot [2/(\pi e)]^{1/2} \cdot (2\rho c)^{-1} \cdot [1/(T_{A1} - T_o) - 1/(T_m - T_o)] \quad (6)$$

Note that Equation 6 describes the separation of the  $T_m$  and  $T_{A1}$  isotherms. The absolute positions of both isotherms are influenced by the effects of poorly known factors such as weld pool convection. However, this formulation eliminates such variations.

### Fraction of Incident Energy Absorbed by the Weld

By rearranging Equation 6,  $A$  can be calculated, based on the width of the HAZ and the process parameters

$$A = (r_{A1} - r_m) \cdot (vd/q) \cdot (\pi e/2)^{1/2} \cdot (2\rho c) \cdot [1/(T_{A1} - T_o) - 1/(T_m - T_o)]^{-1} \quad (7)$$

$A$  is then used to calculate the energy absorbed by the weld.

### Metallurgy of the Weld HAZ

Metallurgical changes in the HAZ are determined by the steel composition and the welding parameters. In the model described below a single composition index has been used to characterize both the hardenability of the coarse-grained

HAZ, and the hardness of individual microstructural phases. Data from an extensive fundamental study into welding of structural steels by Inagaki and Sekiguchi (Ref. 24) have been used to calibrate the model. These data, which are obtained from steels of similar composition to those investigated here, are relevant to the austenitizing temperature of the coarse-grained HAZ of laser beam welds. The compositional limits within which the data were obtained are given in Table 3.

### Phase Transformations in the HAZ

Various empirical formulas have been proposed to express the effect of alloying elements, relative to that of carbon, on the hardenability, cold cracking susceptibility, or mechanical properties of a welded steel (Ref. 25). They differ in the range of composition and cooling rate over which they were established. A simple formula is adopted here, which characterizes microstructural transformation in the coarse-grained HAZ of carbon manganese steels (Ref. 24):

$$C_{eq} = C + Mn/12 + Si/24 \quad (8)$$

Element symbols refer to nominal steel composition in wt-%.

The products of austenite transformation on cooling are determined by the intersection of the cooling curve with the various phase boundaries in the relevant CCT (continuous cooling transformation) diagram. Characteristic cooling times between  $800^\circ$  and  $500^\circ\text{C}$  can be defined, which result in HAZ microstructures containing: 100% martensite ( $\Delta t_m^{100}$ ); 50% martensite ( $\Delta t_m^{50}$ ); 0% martensite ( $\Delta t_m^0$ ); 0% ferrite ( $\Delta t_f^0$ ); 0% pearlite ( $\Delta t_p^0$ ); 50% bainite ( $\Delta t_b^{50}$ ) and 0% bainite ( $\Delta t_b^0$ ). Figure 1 is a map which illustrates

**Table 3 — Compositional Limits of Validity for Hardness Model (wt-%)**

C		Si		Mn		P		S		Cr		Ni		Cu	
min	max	min	max	min	max	min	max	min	max	min	max	min	max	min	max
0.1	0.18	0.01	0.53	0.41	1.40	0.008	0.029	0.007	0.043	0.02	0.07	0.02	0.06	0.06	0.21





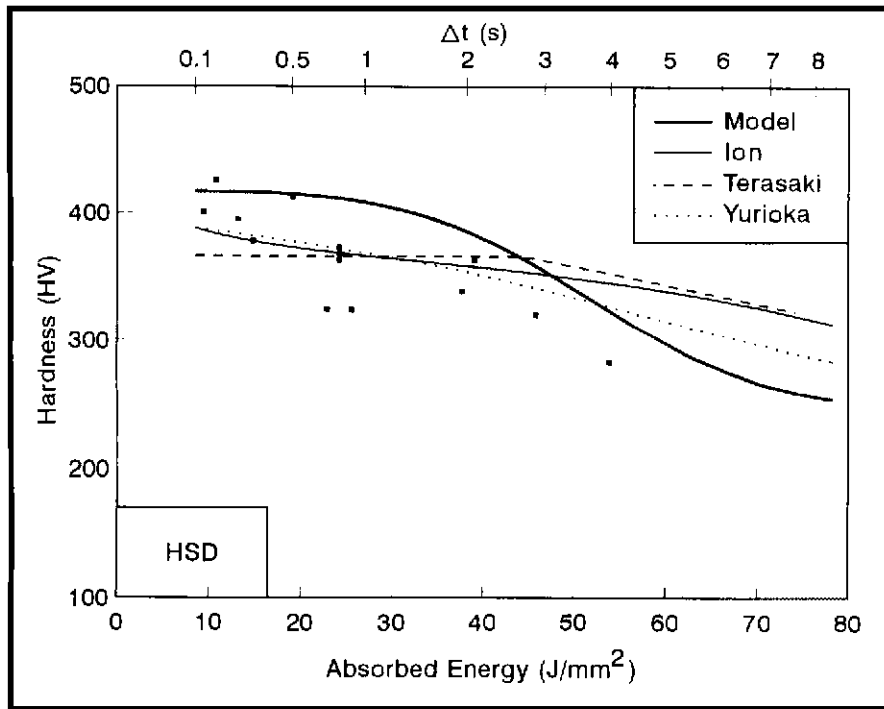


Fig. 4 — Maximum HAZ hardness plotted against absorbed energy for laser welding of the steel HSD. Experimental data, and the predictions of both the present model and more sophisticated models (Refs. 14–16), are shown.

to the absorbed energy. The observed variation in hardness corresponds to microstructures spanning fully martensitic to 100% ferrite/pearlite. The range of absorbed energy is typical of that used in laser welding of plate thicknesses between 4 and 8 mm (0.16 and 0.31 in.).

### Process Diagrams

#### Laser Power - Welding Speed

Figure 6 shows an example of a practical version of a diagram which includes laser welding data for 6 mm (0.24 in.)

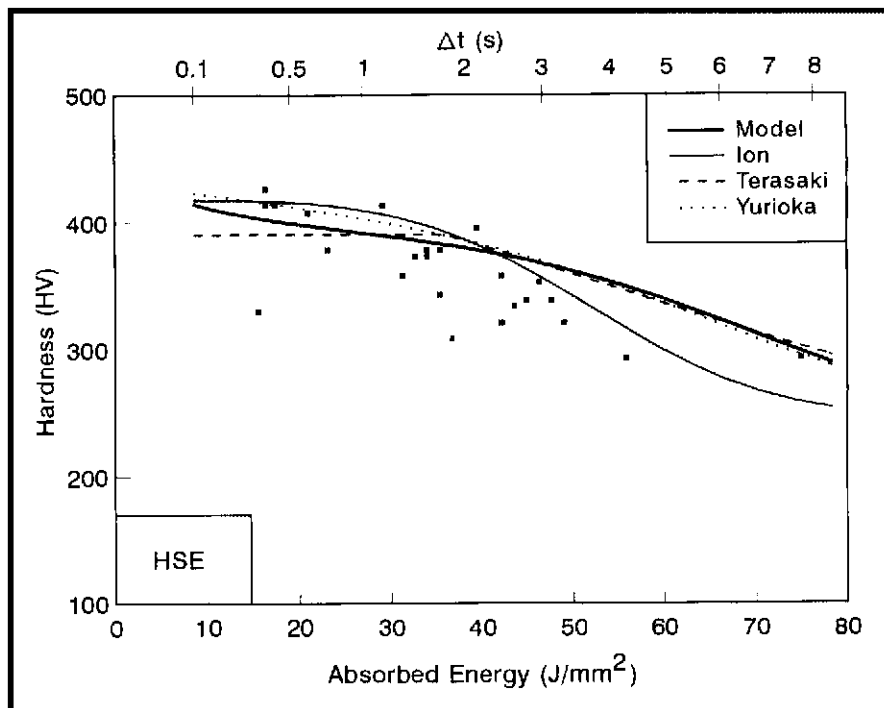


Fig. 5 — Maximum HAZ hardness plotted against absorbed energy for laser beam welding of the steel HSE. Experimental data, and the predictions of both the present model and more sophisticated models (Refs. 14–16), are shown.

Fe52D). The axes of the diagram are the welding parameters normally varied in practice: incident laser power and welding speed. The weldability lobe for full penetration with the particular welding setup used is obtained from empirical data. The contours of constant hardness are constructed using the present model, assuming an average value for absorptivity of 70% in order to convert incident power to absorbed power. Experimental data are plotted and labeled with maximum hardness values. The theoretical maximum contours are seen to overestimate maximum HAZ hardness slightly. The diagram allows practical welding parameters to be selected for a given steel, plate thickness and laser welding setup, based on criteria of full penetration and a maximum permitted HAZ hardness. Similar diagrams can be constructed readily for other steels and plate thicknesses using the PC-based model.

### Steel Composition - Welding Parameters

By using a single carbon equivalent to characterize hardenability and phase hardness, the index may be used as the axis of a diagram which summarizes full penetration welding data for a range of carbon manganese steels and welding parameters. Figure 7 shows such a diagram with axes of carbon equivalent and absorbed energy, with an upper abscissa of cooling time. The contours of constant hardness are constructed using the model described. The experimental data listed in Table 4 are included, labeled with values of maximum hardness. The theoretical contours can be seen to overestimate maximum hardness slightly, and may be used to select steel composition and welding parameters in order to avoid exceeding a maximum HAZ hardness of, e.g., 350 HV. This type of presentation provides an overview of the effects of variations in composition and welding parameters on hardness, for a range of steels within a given class.

### Discussion

#### Prediction of HAZ Hardness

##### Conventional Steels

Figures 2 and 3 show that the present model predicts maximum HAZ hardness in Fe.37B and Fe52D to within approximately 10% of values obtained using the more sophisticated models (Refs. 14–16), over the complete range of HAZ microstructure. Since the carbon equivalent used in the present model is based only on the concentrations of carbon, manganese and silicon, and the concentra-



hardness of laser beam welds, in both the low-alloy carbon-manganese steels, and the thermomechanically processed steels investigated.

2) The explicit nature of the model provides a graphical framework in which to present model predictions as well as experimental data. The practical processing diagram allows the effects of changes in beam power and welding speed on weld properties to be displayed for a given steel, plate thickness and welding setup. The overview diagram, constructed using physically based variable groups, summarizes a large amount of processing data.

3) The diagrams provide guidance at the initial stage of procedure qualification testing of laser welds. Their analytical, explicit nature is also suitable for on-line adaptive control systems, and educational purposes.

4) The techniques described can be sophisticated to take into account the effects of grain growth and further alloying additions, and may be applied to similar deep penetration joining processes such as electron beam welding.

#### Acknowledgments

The assistance of Mr. Pertti Kokko in performing the laser beam welding, and Mr. Esko Reinikainen for metallography is gratefully acknowledged. Financial support was provided by the Technology Development Center of Finland (TEKES).

#### References

1. Rosenthal, D. 1946. The theory of mov-

ing sources of heat and its application to metal treatments. *Trans. ASME* 68: 849-866.

2. Adams, C. M., Jr. 1958. Cooling rates and peak temperatures in fusion welding. *Welding Journal* 35: 210-s to 215-s.

3. Swift-Hook, D. T., and Gick, A. E. F. 1973. Penetration welding with lasers. *Welding Journal* 52: 492-s to 499-s.

4. Cline, H. E., and Anthony, T. R. 1977. Heat treating and melting material with a scanning laser or electron beam. *Journal of Applied Physics* 48: 3895-3900.

5. Rykalin, N., Uglov, A., and Kokora, A. 1978. *Laser Machining and Welding*, Chapter 3, Oxford, England, Pergamon Press.

6. Ashby, M. F., and Easterling, K. E. 1982. A first report on diagrams for grain growth in welds. *Acta Metallurgica* 30:1969-1978.

7. Dowden, J., Davis, M., and Kapadia, P. 1985. The flow of heat and the motion of the weld pool in penetration welding with a laser. *Journal of Applied Physics* 57:4474-4479.

8. Tsai, M. C., and Kou, S. 1988. Laser beam welding — a general line heat source solution. *Proc. Int. Power Beam Conf.*, eds. E. A. Metzbower and D. Hauser, ASM International, pp. 131-140.

9. Mazumder, J., and Steen, W. M. 1980. Heat transfer model for CW laser material processing. *Journal of Applied Physics* 51: 941-947.

10. Kou, S. 1981. Simulation of heat flow during the welding of thin plates. *Metallurgical Transactions* 12A: 2025-2030.

11. Eager, T. W., and Tsai, N. 1983. Temperature fields produced by traveling distributed heat sources. *Welding Journal* 62: 346-s to 355-s.

12. Goldak, J., Chakravarti, A., and Bibby, M. 1984. A new finite element model for welding heat sources. *Metallurgical Transactions* 15B: 299-305.

13. Matsuhira, Y., Inaba, Y., and Ohji, T. 1994. Mathematical modelling of laser welding with a keyhole: modelling of laser welding (part 1). *Welding International* 8: 286-291.

14. Terasaki, T. 1981. Study of predictive equations of thermal factor and hardness re-

lated with weld cold cracking. *Journal of the Iron and Steel Institute of Japan* 16:145-152.

15. Ion, J. C., Easterling, K. E., and Ashby, M. F. 1984. A second report on diagrams of microstructure and hardness for heat-affected zones in welds. *Acta Metallurgica* 32:1949-1962.

16. Yurioka, N., Okumura, M., Kasuya, T., and Cotton, H. J. U. 1987. Prediction of HAZ hardness of transformable steels. *Metal Construction* 19: 217R-223R.

17. Henwood, C., Bibby, M., Goldak, J., and Watt, D. 1988. Coupled transient heat transfer microstructural weld computations (Part B). *Acta Metallurgica* 36: 3037-3046.

18. Watt, D. F., Coon, L., Bibby, M., Goldak, J. and Henwood, C. 1988. Modelling microstructural development in weld heat-affected zones (Part A) reaction kinetics. *Acta Metallurgica* 36: 3029-3035.

19. Buchmayr, B. 1990. Modelling of microstructural changes during welding of HSLA steels. *Proc. 3rd Int. Conf. Computer Technology in Welding*, Abington Publishing, Cambridge, U.K., pp. 162-171.

20. Metzbower, E. A. 1990. Laser beam welding: thermal profiles and HAZ hardness. *Welding Journal* 69: 272-s to 278-s.

21. Edwards, A. L. 1969. For Computer Heat Conduction Equations — A Compilation of Thermal Properties Data, Report UCRL-50589, Feb. 24 1969.

22. Andrews, K. W. 1965. Empirical formulae for the calculation of some transformation temperatures. *Journal of the Iron and Steel Institute* 203: 721-727.

23. Smithells, C. M. 1976. *Metals Reference Book*, 5th edn, p. 510; London, Butterworths.

24. Inagaki, M., and Sekiguchi, H. 1960. Continuous cooling transformation diagrams of steels for welding and their applications. *Transactions of the National Research Institute for Metals, Japan* 2:102-125.

25. Hrivnák, I. 1978. The mutual relationship and interdependence of developments in steel metallurgy and welding technology. *Welding in the World* 16:130-151.